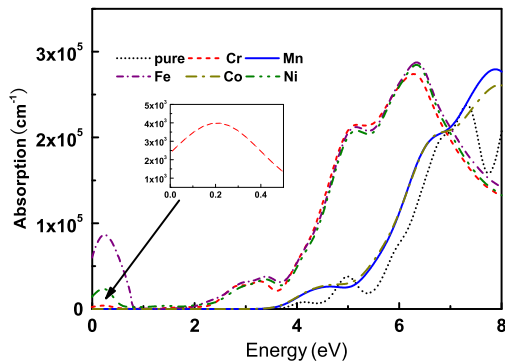


CONTENTS

Abstracted/indexed in BioEngineering Abstracts, Chemical Abstracts, Coal Abstracts, Current Contents/Physics, Chemical, & Earth Sciences, Engineering Index, Research Alert, SCISEARCH, Science Abstracts, and Science Citation Index. Also covered in the abstract and citation database SCOPUS®. Full text available on ScienceDirect®.

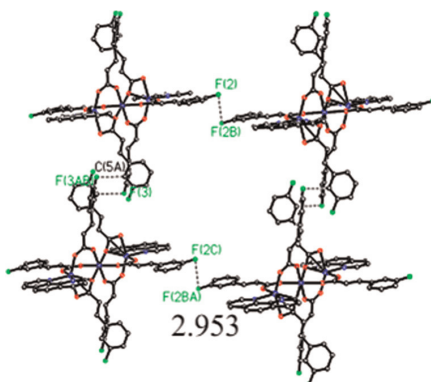
Regular Articles

Infrared, visible and ultraviolet absorptions of transition metal doped ZnS crystals with spin-polarized bands
 J.H. Zhang, J.W. Ding, J.X. Cao and Y.L. Zhang
page 477



Absorption coefficients of ω - $TM_xZn_{1-x}S$ crystals ($TM=Cr^{2+}$, Mn^{2+} , Fe^{2+} , Co^{2+} and Ni^{2+}) at $x=0.028$. The results may be helpful for the design and applications of TM :ZnS devices, especially for the new high efficiency solar-cell prototype, UV detector and UV LEDs.

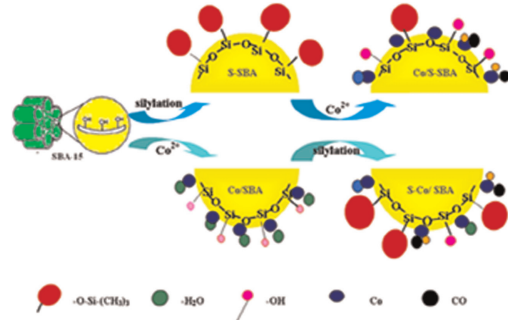
The C–F...F–C short contacts in the metal complexes of fluoro-phenyl-acrylic acids
 Gui-lei Liu, Cai-Ming Liu and Hui Li
page 481



The short distance between $F \dots F$ (2.953 Å) was found in the complex of $[Mn_3(L1)_6(L2)_2] \cdot H_2O \cdot CH_3CN$ ($L1=(E)-3-(3$ -fluorophenyl)-acrylic acid, $L2=1,10$ -phenanthroline).

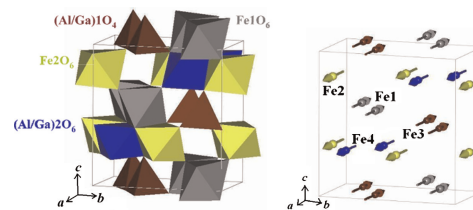
Regular Articles—Continued

Silylated Co/SBA-15 catalysts for Fischer–Tropsch synthesis
 Lihong Jia, Litao Jia, Debao Li, Bo Hou, Jungang Wang and Yuhan Sun
page 488



The silylation of an SBA-15 before cobalt impregnation enhanced the reducibility of cobalt oxides on an SBA-15-supported cobalt catalyst and consequently increased the catalytic activity for Fischer–Tropsch synthesis.

Structure and magnetic properties of the $Al_{1-x}Ga_xFeO_3$ family of oxides: A combined experimental and theoretical study
 Rana Saha, Ajmala Shireen, A.K. Bera, Sharmila N. Shirodkar, Y. Sundarayya, Nandakumar Kalarikkal, S.M. Yusuf, Umesh V. Waghmare, A. Sundaresan and C.N.R Rao
page 494

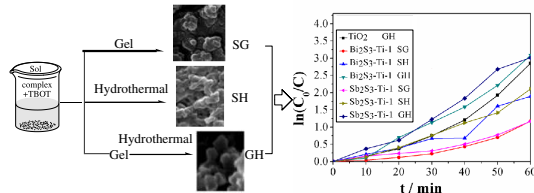


We have studied both experimentally and theoretically the important role of disorder at the cation site on magnetic and related properties of the $Al_{1-x}Ga_xFeO_3$ family of oxides crystallizing in a non-centrosymmetric space group.

Continued

Preparation and photocatalytic activity of $\text{Sb}_2\text{S}_3/\text{Bi}_2\text{S}_3$ doped TiO_2 from complex precursor via gel–hydrothermal treatment

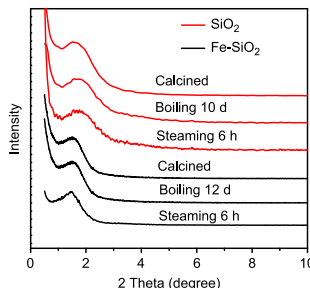
Yan Huang, Gang Xie, Sanping Chen and Shengli Gao
page 502



$\text{Sb}_2\text{S}_3/\text{Bi}_2\text{S}_3$ doped TiO_2 were prepared using $[M(\text{S}_2\text{COEt})_3]$ ($M = \text{Sb, Bi}$; S_2COEt = pyridine-1-dithiocarbamate) as precursors via gel–hydrothermal techniques. M_2S_3 doped TiO_2 performs better photocatalytic activity for photodegradation reaction of 4-nitrophenol.

High-temperature synthesis of highly hydrothermal stable mesoporous silica and $\text{Fe}-\text{SiO}_2$ using ionic liquid as a template

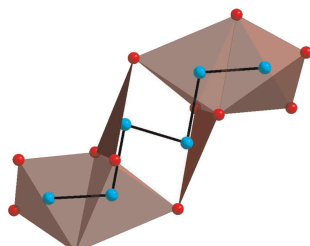
Hong Liu, Mengyang Wang, Hongjiu Hu, Yuguang Liang, Yong Wang, Weiran Cao and Xiaohong Wang
page 509



Worm-like mesoporous silica and $\text{Fe}-\text{SiO}_2$ with high hydrothermal stability have been synthesized using ionic liquid 1-hexadecane-3-methylimidazolium bromide as a template under the assistance of NaF at high temperature.

Synthesis, crystal and electronic structure, and physical properties of the new lanthanum copper telluride $\text{La}_3\text{Cu}_5\text{Te}_7$

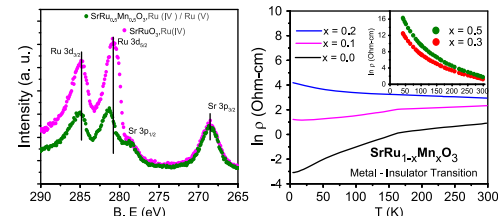
Mariya Zelinska, Abdeljalil Assoud and Holger Kleinke
page 516



Oligomeric unit comprising interconnected CuTe_3 pyramids and CuTe_4 tetrahedra.

Valence and origin of metal–insulator transition in Mn doped SrRuO_3 studied by electrical transport, X-ray photoelectron spectroscopy and LSDA + U calculation

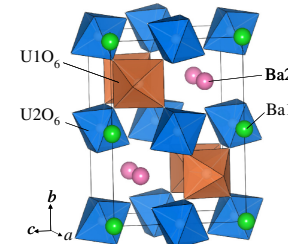
Ranjan K. Sahu, Sudhir K. Pandey and L.C. Pathak
page 523



XPS data and electrical transport data show that doping of Mn in metallic SrRuO_3 induces mixed ionic pair $\text{Ru}(\text{IV})/\text{Ru}(\text{V}) \leftrightarrow \text{Mn}(\text{III})/\text{Mn}(\text{IV})$ and the system undergoes a transition from metal to insulator at the critical Mn doping level, $x \sim 0.2$. The origin for the metal–insulator transition has been discussed.

Magnetic properties of barium uranate $\text{Ba}_2\text{U}_2\text{O}_7$

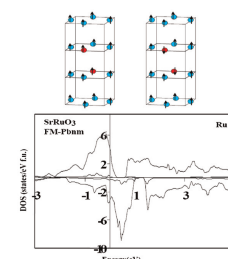
Akio Nakamura, Yoshihiro Doi and Yukio Hinatsu
page 531



Magnetic susceptibility, magnetization, and specific heat measurements reveal that $\text{Ba}_2\text{U}_2\text{O}_7$ undergoes a canted antiferromagnetic ordering at 19 K. In addition, another magnetic anomaly is observed at 58 K, which may be due to one-dimensional magnetic correlations of the U ions.

Ferromagnetism and antiferromagnetism coexistence in $\text{SrRu}_{1-x}\text{Mn}_x\text{O}_3$: Density functional calculation

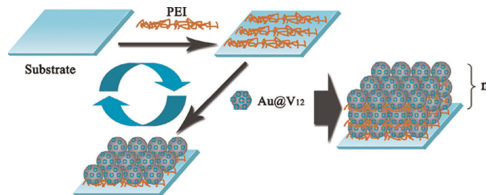
H. Hadipour, S. Fallahi and M. Akhavan
page 536



The antiparallel alignment between the Mn and Ru ions are consistent with the competition between ferromagnetism and antiferromagnetism with the formation of a spin glass phase. We have calculated the electronic structure of $\text{SrRu}_{1-x}\text{Mn}_x\text{O}_3$ using the full potential linearized augmented plane wave method by LSDA and LSDA + U in the range of both low and high Mn-doping for parallel and antiparallel alignments of Ru and Mn moments. In the low Mn-doped polycrystalline samples with tetragonal structure, the AFM hybridization between Mn and the Ru host lattice strongly favors alignment of the Ru moments, and provides an explanation for retaining of high Curie temperature of SrRuO_3 with Mn substitution.

One-step synthesis and stabilization of gold nanoparticles and multilayer film assembly

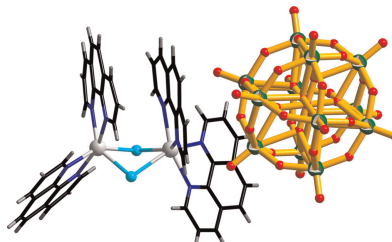
Ya-Yan Bao, Li-Hua Bi and Li-Xin Wu
page 546



The wheel-shaped $V^V\text{-}V^{IV}$ mixed-valence tungstovanadate $[\text{P}_8\text{W}_{48}\text{O}_{184}\{\text{V}_4\text{V}_1\text{O}_{12}(\text{H}_2\text{O})_2\}_2]^{32-}$ (V12) stabilized Au nanoparticles (Au@V12 NPs) have been synthesized and characterized. The multilayer films containing Au@V12 NPs were fabricated and their electrocatalytic properties were studied.

Two new hybrid compounds assembled from Keggin-type polyoxometalates and transition metal coordination complexes

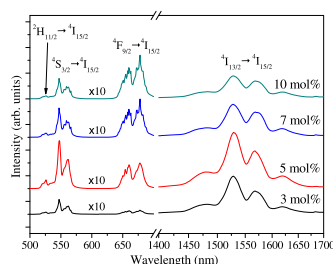
Yan Wang, Bo Zou, Li-Na Xiao, Ning Jin, Yu Peng, Feng-Qing Wu, Hong Ding, Tie-Gang Wang, Zhong-Min Gao, Da-Fang Zheng, Xiao-Bing Cui and Ji-Qing Xu
page 557



Two new hybrid compounds based on different Keggin-type polyoxometalates have been hydrothermally synthesized and characterized by IR, UV-Vis, XPS, XRD, elemental analysis and single crystal X-ray diffraction analysis.

Visible and infrared luminescence properties of Er^{3+} -doped $\text{Y}_2\text{Ti}_2\text{O}_7$ nanocrystals

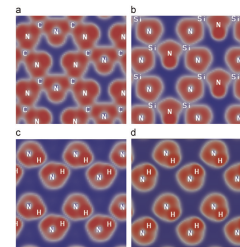
Chu-Chi Ting, Yi-Shan Chiu, Chia-Wei Chang and Liang-Chih Chuang
page 563



Emission fluorescence spectra of the Er^{3+} (3, 5, 7, or 10 mol%)-doped $\text{Y}_2\text{Ti}_2\text{O}_7$ nanocrystals annealed at 800 °C for 1 h under 980 nm pumping. The Er^{3+} -doped $\text{Y}_2\text{Ti}_2\text{O}_7$ nanocrystals absorbing 980 nm photons can produce the upconversion (526, 547, and 660 nm; $^2\text{H}_{11/2} \rightarrow ^4\text{I}_{15/2}$, $^4\text{S}_{3/2} \rightarrow ^4\text{I}_{15/2}$, and $^4\text{F}_{9/2} \rightarrow ^4\text{I}_{15/2}$, respectively) and Stokes (1528 nm; $^4\text{I}_{13/2} \rightarrow ^4\text{I}_{15/2}$) photoluminescence.

Low-compressibility and hard material carbon nitride imide $\text{C}_2\text{N}_2(\text{NH})$: First principles calculations

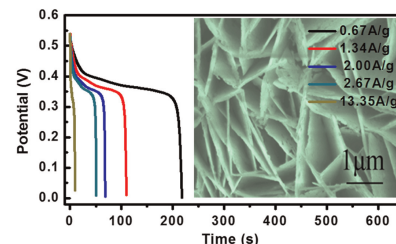
Hai-Yan Yan, Qun Wei, Bao-bing Zheng and Ping Guo
page 572



Contours of electronic localization function (ELF) of $\text{C}_2\text{N}_2(\text{NH})$ on the: (0 0 1) plane (a), (1 0 0) plane (b), an ELF of $\text{Si}_2\text{N}_2(\text{NH})$ on the: (0 0 1) plane (c) and (1 0 0) plane (d).

Direct synthesis of porous NiO nanowall arrays on conductive substrates for supercapacitor application

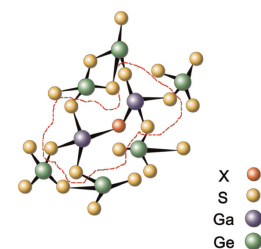
Jianhui Zhu, Jian Jiang, Jingping Liu, Ruimin Ding, Hao Ding, Yamin Feng, Guangming Wei and Xintang Huang
page 578



Porous NiO nanowall arrays (NWAs) grown on alloy substrate have been made using nullaginite as precursor and studied as supercapacitor electrodes. Porous nanowalls interconnected with each other resulting in the formation of extended-network architectures and exhibited excellent capacitor properties. NiO NWAs electrode delivered a capacitance of 270 F/g (0.67 A/g); even at high current density, the electrode could still deliver a high capacitance up to 236 F/g (13.35 A/g). Besides, it exhibited excellent cycle lifetime with ~93% capacitance kept after 4000 cycles. These remarkable results made it possible for mass production of NiO NWAs and future thin-film microelectronic applications.

Evidence of network demixing in $\text{GeS}_2\text{-}\text{Ga}_2\text{S}_3$ chalcogenide glasses: A phase transformation study

Changgui Lin, Laurent Calvez, Haizheng Tao, Mathieu Allix, Alain Moréac, Xianghua Zhang and Xujian Zhao
page 584

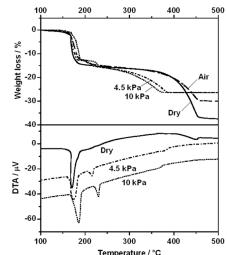


Synopsis: network demixing in $\text{GeS}_2\text{-}\text{Ga}_2\text{S}_3$ chalcogenide glasses.

Continued

Effect of water vapor on the thermal decomposition process of zinc hydroxide chloride and crystal growth of zinc oxide
Takahiro Kozawa, Ayumu Onda, Kazumichi Yanagisawa, Akira Kishi and Yasuaki Masuda

page 589

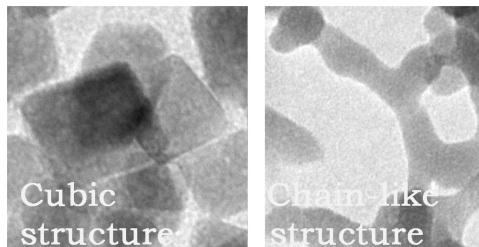


Thermal decomposition process of zinc hydroxide chloride (ZHC), $Zn_5(OH)_8Cl_2 \cdot H_2O$, has been investigated by novel thermal analyses with three different water vapor partial pressures. In the water vapor atmosphere, the formation of ZnO was completed at lower temperatures than in dry.

Effects of surfactants on morphology in synthesis of α -Mn₂O₃ nanostructures

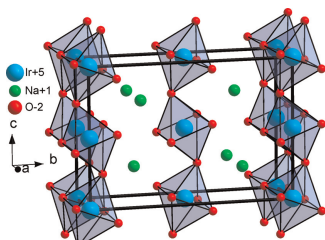
D. Ramarajan and P. Sivagurunathan

page 597



Cubic and chain-like nanostructure of α -Mn₂O₃ has been synthesized by air oxidation of manganese chloride as precursor, hexamine, and mercaptosuccinic acid as wetting agent, respectively.

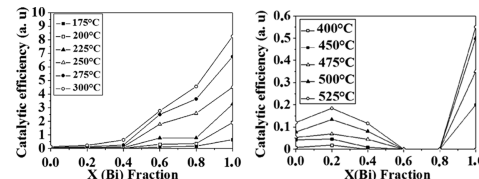
NaIrO₃—A pentavalent post-perovskite
M. Bremholm, S.E. Dutton, P.W. Stephens and R.J. Cava



Sodium iridium(V) oxide, NaIrO₃, synthesized by a high pressure solid state method and recovered to ambient conditions is found to crystallize as the post-perovskite structure and is the first example of a pentavalent ABO₃ post-perovskite.

Structural, microstructural and surface properties of a specific CeO₂–Bi₂O₃ multiphase system obtained at 600 °C
Lamia Bourja, Bahcine Bakiz, Abdeljalil Benlhachemi, Mohamed Ezahri, Sylvie Villain, Olivier Crosnier, Claude Favotto and Jean-Raymond Gavarri

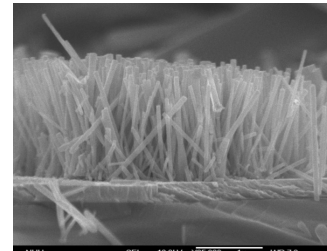
page 608



Catalytic efficiencies of CeO₂–Bi₂O₃ system: catalytic actions on methane (on the left) or carbon monoxide (on the right) of $(1-x)CeO_2-x/2 Bi_2O_3$ samples, as a function of the fraction x , and for fixed temperatures: on the vertical axis, the intensities of CO₂ FTIR absorption bands are reported. Strong efficiency of bismuth rich samples for CO conversion.

Optimization of processing parameters on the controlled growth of ZnO nanorod arrays for the performance improvement of solid-state dye-sensitized solar cells
Yi-Mu Lee and Hsi-Wen Yang

page 615

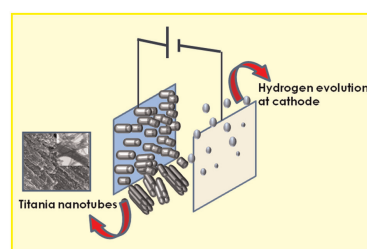


The ZnO nanorod arrays demonstrate well-alignment, high aspect ratio ($L/D \sim 21$) and excellent optical transmittance by low-temperature chemical bath deposition (CBD).

Rapid breakdown anodization technique for the synthesis of high aspect ratio and high surface area anatase TiO₂ nanotube powders

Rajini P. Antony, Tom Mathews, Arup Dasgupta, S. Dash, A.K. Tyagi and Baldev Raj

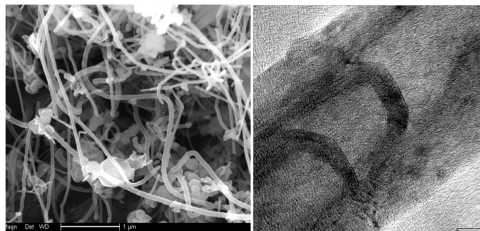
page 624



Catalytic synthesis of bamboo-like multiwall BN nanotubes via SHS-annealing process

L.P. Zhang, Y.L. Gu, J.L. Wang, G.W. Zhao, Q.L. Qian, J. Li, X.Y. Pan and Z.H. Zhang

page 633

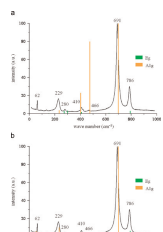


A novel and effective annealing porous precursor route to bulk synthesis of bamboo-like multiwall BN nanotubes. Four growth models of VLS growth mechanism for these nanotubes are proposed.

Crystal chemistry peculiarities of $\text{Cs}_2\text{Te}_4\text{O}_{12}$

David Hamani, Andréi Mirgorodsky, Olivier Masson, Thérèse Merle-Méjean, Maggy Colas, Mikhael Smirnov and Philippe Thomas

page 637

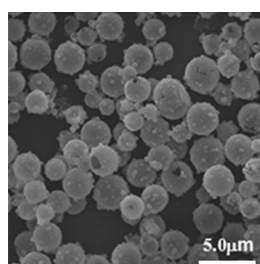


Two versions of the BPM estimations of the Raman intensity for the $\text{Cs}_2\text{Te}_4\text{O}_{12}$ lattice vibrations: (a) without including effects of the Cs-O bonds and (b) including the above mentioned effects. Experimentally observed peaks are characterized by their frequency positions.

Photochemical preparation of CdS hollow microspheres at room temperature and their use in visible-light photocatalysis

Yuying Huang, Fengqiang Sun, Tianxing Wu, Qingsong Wu, Zhong Huang, Heng Su and Zihe Zhang

page 644

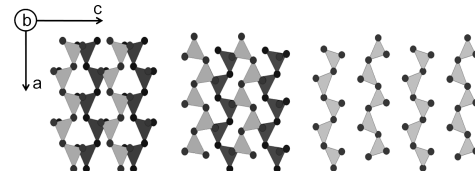


Taking polystyrene spheres dispersed in a precursor solution as templates, CdS hollow microspheres composed of nanoparticles were successfully prepared via a new photochemical route at room temperature.

Crystallographic and magnetic characterisation of the brownmillerite $\text{Sr}_2\text{Co}_2\text{O}_5$

Eirin Sullivan, Joke Hadermann and Colin Greaves

page 649

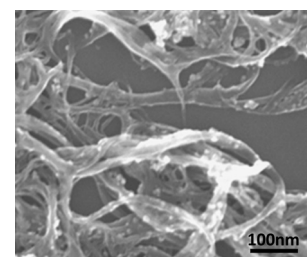


Possible ordering of the tetrahedral chains in $\text{Sr}_2\text{Co}_2\text{O}_5$.

Study of the surface chemistry and morphology of single walled carbon nanotube–magnetite composites

F. Marquez-Linares, O.N.C. Uwakweh, N. Lopez, E. Chavez, R. Polanco, C. Morant, J.M. Sanz, E. Elizalde, C. Neira, S. Nieto and R. Roque-Malherbe

page 655

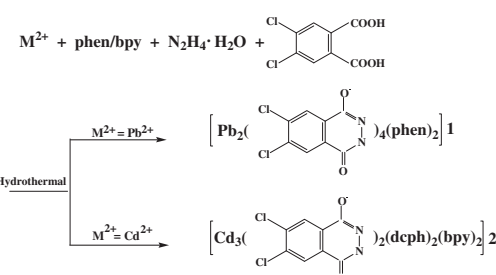


A large amount of Lewis acid sites were found in the highly dispersed magnetite which is supported on the SWCNT outer surface.

New 4,5-dichlorophthalhydrazide-bridged chained coordination polymers

Juan Jin, Ming-Jun Jia, Yu Peng, Jie-Hui Yu, Yu-Chang Wang and Ji-Qing Xu

page 667

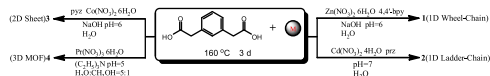


By applying the *in situ* acylation reaction between 4,5-dichlorophthalic acid and $\text{N}_2\text{H}_4 \cdot \text{H}_2\text{O}$, two 4,5-dichlorophthalhydrazide-bridged chained compounds $[\text{Pb}_2(\text{DCPTH})_4(\text{phen})_2]$ and $[\text{Cd}_3(\text{DCPTH})_2(\text{dcpb})_2(\text{bpy})_2]$ (4,5-dichlorophthalhydrazide = DCPTH, and dcpb = 4,5-dichlorophthalate) were hydrothermally synthesized.

Continued

Synthesis, structures, luminescent and magnetic properties of four coordination polymers with the flexible 1,3-phenylenediacetate ligands

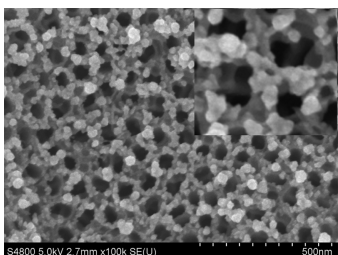
Jin-Zhong Gu, Dong-Yu Lv, Zhu-Qing Gao, Jian-Zhao Liu, Wei Dou and Yu Tang
page 675



Four new coordination polymers with 1,3-phenylenediacetate ligands have been hydrothermally synthesized and characterized. Complexes **1** and **2** display strong blue fluorescent emission at room temperature. Magnetic susceptibility measurements of **3** and **4** exhibit antiferromagnetic interactions between the nearest metal centers.

Fabrication and photocatalytic activity of high-efficiency visible-light-responsive photocatalyst ZnTe/TiO₂ nanotube arrays

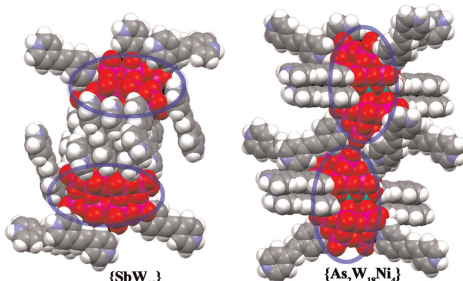
Yutang Liu, Xilin Zhang, Ronghua Liu, Renbin Yang, Chengbin Liu and Qingyun Cai
page 684



Surface-view SEM images of ZnTe/TiO₂ NT prepared under -2.0 V, and the inset is the corresponding enlarged drawings.

Assemblies based on the directing effect of non-classical W₁₈ anionic clusters and the rod-like trans-1,2-di-(4-pyridyl)-ethylen (bpe)

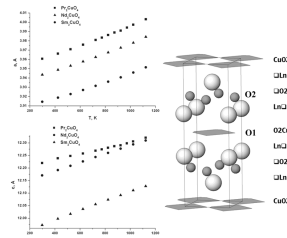
Zhangang Han, Yanna Wang, Xuejun Song, Jiao Huang and Xueliang Zhai
page 690



Two polyoxometalate-based supramolecular assemblies built upon W₁₈ clusters and the rigid organic trans-1,2-di-(4-pyridyl)-ethylen (bpe) have been synthesized and characterized.

High-temperature crystal structure and transport properties of the layered cuprates *Ln*₂CuO₄, *Ln*=Pr, Nd and Sm

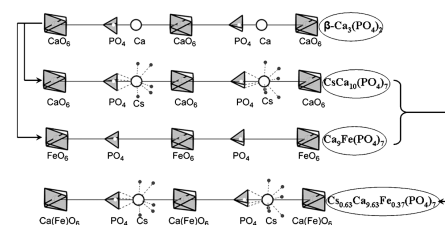
M.S. Kaluzhskikh, S.M. Kazakov, G.N. Mazo, S.Ya. Istomin, E.V. Antipov, A.A. Gippius, Yu. Fedotov, S.I. Bredikhin, Yi Liu, G. Svensson and Z. Shen
page 698



Anomaly anisotropic thermal expansion behavior was observed for Pr₂CuO₄ in comparison with *Ln*₂CuO₄, *Ln*=Pr and Nd having tetragonal T'-structure with thermal expansion coefficients (TEC) along *a*- and *c*-axis changing from TEC(*a*)/TEC(*c*)≈1.37 (Pr) to 0.89 (Nd) and 0.72 (Sm). It was found that the trace diffusion coefficient (*D*_T) of oxygen in Pr₂CuO₄ determined by secondary ion mass spectrometry (SIMS) varies in the range 7.2×10⁻¹³ cm²/s (973 K) and 3.8×10⁻¹⁰ cm²/s (1173 K) which are in between those observed for the manganese and cobalt-based perovskites.

Synthesis and characterization of phosphates in molten systems Cs₂O-P₂O₅-CaO-*M*^{III}O₃ (*M*^{III}=Al, Fe, Cr)

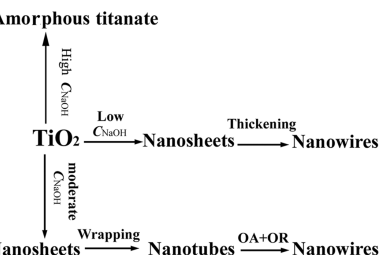
Igor V. Zatovsky, Nataliya Yu. Strutynska, Vyacheslav N. Baumer, Nikolay S. Slobodyanik, Ivan V. Ogorodnyk and Oleg V. Shishkin
page 705



Structural relationships between β-Ca₃(PO₄)₂ and synthesized compounds is shown in terms aliovalent substitution of calcium atoms, which residue on three-fold axis, by other metals in β-Ca₃(PO₄)₂ framework.

Formation of titanate nanostructures under different NaOH concentration and their application in wastewater treatment

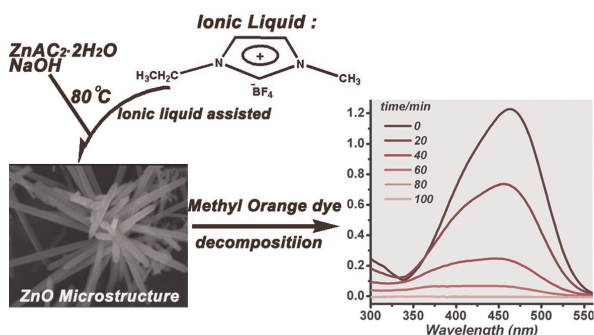
Jiquan Huang, Yongge Cao, Zhonghua Deng and Hao Tong
page 712



The morphologies of the titanates depend deeply on the concentration of NaOH. With increasing NaOH concentration, three different formation mechanisms were proposed. The application of these titanate nanostructures in the wastewater treatment was studied.

Microbundles of zinc oxide nanorods: Assembly in ionic liquid $[\text{EMIM}]^+[\text{BF}_4]^-$, photoluminescence and photocatalytic properties

Li Wang, Shen-Zhi Xu, Hui-Jun Li, Li-Xian Chang, Zhi-Su, Ming-Hua Zeng, Li-Na Wang and Yi-Neng Huang
page 720



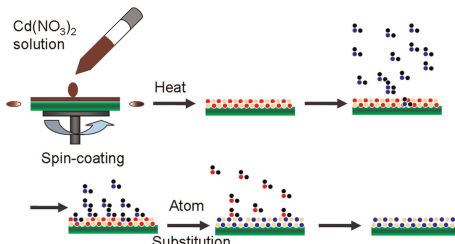
Easy formation of microbundles of ZnO nanorods were accomplished in low temperature with $[\text{EMIM}]^+[\text{BF}_4]^-$ (1-ethyl-3-methylimidazolium tetrafluoroborate) ionic liquid, which exhibit significant green-yellow photoluminescence property and high photodegradation of Methyl Orange dye.

Rapid Communication

CdS thin films on LiNbO_3 (1 0 4) and silicon (1 1 1) substrates prepared through an atom substitution method

Haiming Qin, Yue Zhao, Hong Liu, Zheng Gao, Jiyang Wang, Duo Liu, Yuanhua Sang, Bin Yao and Robert I. Boughton

page 725



Elemental O in CdO is substituted by elemental S from the atmosphere in the apparatus, which is designated as an atom substitution process. This novel method involving an atom substitution reaction between the CdO precursor thin film and its environment can provide a new low cost approach to the preparation of chalcogenide or other compound thin films.

Author inquiries

For inquiries relating to the submission of articles (including electronic submission where available) please visit this journal's homepage at <http://www.elsevier.com/locate/jssc>. You can track accepted articles at <http://www.elsevier.com/trackarticle> and set up e-mail alerts to inform you of when an article's status has changed. Also accessible from here is information on copyright, frequently asked questions and more. Contact details for questions arising after acceptance of an article, especially those relating to proofs, will be provided by the publisher.

Language services. Authors who require information about language editing and copyediting services pre- and post-submission please visit <http://webshop.elsevier.com/languageediting> or our customer support site at <http://support.elsevier.com>. Please note Elsevier neither endorses nor takes responsibility for any products, goods or services offered by outside vendors through our services or in any advertising. For more information please refer to our Terms & Conditions <http://www.elsevier.com/termsandconditions>

For a full and complete Guide for Authors, please go to: <http://www.elsevier.com/locate/jssc>

Journal of Solid State Chemistry has no page charges.